J. Biophotonics **4**, No. 3, 184–192 (2011) / **DOI** 10.1002/jbio.201000096

Journal of BIOPHOTONICS

FULL ARTICLE

# Interferometric fiber optic sensors for biomedical applications of optoacoustic imaging

*Horacio Lamela*[*,1], *Daniel Gallego*[1], *Rebeca Gutierrez*[1], *and Alexander Oraevsky*[2]

[1] Universidad Carlos III de Madrid, 28911 Leganes, Madrid, Spain
[2] TomoWave Laboratories, Inc. Houston, Texas 77057, USA

Received 8 September 2010, revised 16 December 2010, accepted 22 December 2010
Published online 18 January 2011

**Key words:** fiber optic sensors, ultrasound, optoacoustic imaging, interferometry

We present a non-metallic interferometric silica optical fiber ultrasonic wideband sensor for optoacoustic imaging applications. The ultrasonic sensitivity of this sensor has been characterized over the frequency range from 1 to 10 MHz. A comparative analysis has been carried out between this sensor and an array of piezoelectric transducers using optoacoustic signals generated from an optical absorbent embedded in a tissue mimicking phantom. Also, a two dimensional reconstructed image of the phantom using the fiber interferometric sensor is presented and compared to the image obtained using the Laser Optoacoustic Imaging System, LOIS-64B. The feasibility of our fiber optic based sensor for wideband ultrasonic detection is demonstrated.

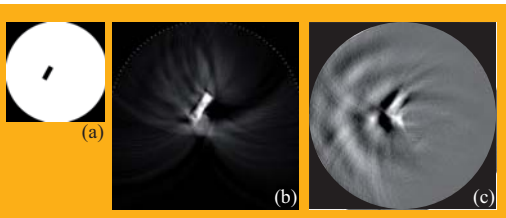


(**a**) Diagram showing location of the embedded object in the PVCP phantom. (**b**) Optoacoustic image obtained from LOIS utilizing an array of 64 PVDF transducers. (**c**) Optoacoustic image reconstructed from fiber optic sensor signals.

## 1. Introduction

Optoacoustic tomography [1, 2] is a promising non-invasive non-ionizing imaging technique that can be used to visualize biological soft tissue. It combines the advantages resulting from high optical absorption contrast in biological tissues with the exceptional spatial resolution of ultrasound imaging techniques. In recent years this imaging method has been used in several biomedical applications such as visualization of blood vessels and the measurement of blood oxygenation [3], detection of tumors in breast tissue [4–6], small animal imaging [7] and functional imaging [8]. The optoacoustic technique is based on the irradiation of the tissue surface with laser pulses of a few nanoseconds operating in the visible or near-infrared wavelengths range. The optical absorption of the laser pulse by the different tissue structures produces an instant distribution of heat sources and, as a result of the thermoelastic effect, broadband ultrasonic pulses are generated. These ultrasonic waves propagate to the surface of the tissue where they are detected using ultrasonic transducers. The typical frequency spectrum of the optoacoustic signals generated at a depth of several centimeters that reach the surface after suffer ultrasonic attenuation of the soft tissue covers a wide range from ~100 kHz to ~10 MHz. The desirable characteristics for ultrasonic transducers used in the detection of optoacoustic signals and for high spatial resolution image reconstruction are high sensitivity and a broadband nature.

* Corresponding author: e-mail: horacio@ing.uc3m.es, Phone: +34 91 624 9476, Fax: +34 91 624 9430

Traditionally, detection technology used in conventional ultrasonic imaging is based on piezoelectric transducers, which are highly sensitive but have a narrow bandwidth resulting from their resonant nature. However the optoacoustic signals generated require broadband detectors to image the different sizes of absorption regions within the body. The detectors based on thin piezoelectric polymer films, like polyvinylidene fluoride (PVDF), can be made sensitive over an ultrawide-band using appropriate backing and front matching materials. However, their sensitivity decreases as their size is reduced. This presents a problem when detecting high ultrasonic frequencies where both the small thickness of the detector, required for high axial resolution, and the small width of the transducer element, required for high lateral resolution and improved image fidelity, reduce its sensitivity. Another drawback to piezoelectric sensors, related to their electrical nature, is that they are not immune to electromagnetic interference.

Over the past 30 years, optical detection of ultrasound has been studied as an alternative to piezoelectric technology. Clear distinctions can be made between two types of ultrasound optical sensors, those that monitor pressure induced displacements of a membrane or resonant optical cavity; and others that are based on a pressure induced index refraction variation in or around the sensor material. In the first group, the following sensors can be found: etalons [9], fiber Bragg gratings [10], and dielectric multilayer interference filters [11]. Intrinsic fiber optic interferometric sensors [12] form part of the second group. All these optical sensors, contrary to piezoelectric transducers, are not affected by external electromagnetic disturbances or other artifacts like electrical noise and thermal signals produced by the direct laser pulse illumination. In particular, the fabrication of intrinsic fiber optic interferometric sensors is straightforward and involves the use of low cost materials. Moreover the sensitivity of these sensors can be improved by appropriate folding or coiling of the fiber [13] which increases the surface area that interacts with the acoustic field.

In this work the principle of operation of the ultrasonic optical fiber interferometric sensor is introduced in Section 2. We present, in Section 3, the characterization of the acoustic sensitivity of the optical fiber used to develop the sensor for the frequency range from 100 KHz to 10 MHz. Also, in this section, we compare the optoacoustic signals detected using this fiber optic interferometric sensor to those obtained using a PVDF transducer. In Section 4, a summary of the back projection algorithm and wavelet processing used to reconstruct optoacoustic images are both introduced. We compare an image obtained from a phantom mimicking soft tissues by this system with other image obtained using an array of piezoelectric transducers made from PVDF [14] in Section 5. Finally, in Section 6, conclusions and future work are presented.

## 2. Principle of fiber optic sensor operation

The operation of an optical fiber interferometric sensor is based on the transduction of the ultrasonic wave by a phase shift of the light traveling through the fiber. By means of a Mach-Zehnder interferometer the phase shift of light is transformed into a variation in the optical intensity. Finally, the optical signal is converted to a voltage signal using a photodiode and a transimpedance amplifier. Considering all these factors, the total sensitivity of the detector, i.e. the relation between the output voltage and the acoustic pressure, may be expressed as

$$\frac{\Delta V}{\Delta P} = \frac{\Delta V}{\Delta I}\,\frac{\Delta I}{\Delta \phi}\,\frac{\Delta \phi}{\Delta P} \tag{1}$$

where $P$ is the acoustic pressure amplitude, $\phi$ is the phase of the light, $I$ is light intensity at the interferometer output and $V$ is the voltage at the output of the transimpedance amplifier.

In general, an acoustic wave that is incident on an optical fiber induces strain, thus producing a refractive index variation that modifies the phase of light, given by $\Delta\varphi = k(n\,\Delta l + l\,\Delta n)$, here $k$ is the laser wave number, $l$ is the length of the sensing segment and $n$ is the effective refractive index of the optical fiber. At ultrasonic frequencies, the induced strain, localized on a fiber segment of length $l$, can be considered axially constrained, thus the phase shift induced is mainly governed by the strain-optic effect taking into account in $l\,\Delta n$ factor. Within the regime $d \ll \lambda_a$, where $d$ is the optical fiber diameter and $\lambda_a$ is the acoustic wavelength, it can be assumed that the acoustic strain has radial symmetry, thus there is no birefringence induced. The effective refractive index perturbation is linear and proportional to the pressure wave magnitude, $P(\vec{r}, t)$:

$$\Delta n(\vec{l}, t) = \alpha P(\vec{r}, t)|_{\vec{r}=\vec{l}} \tag{2}$$

Where $\alpha$ is a proportional constant that depends on the acoustic coupling conditions, Young's modulus, the Poisson ratio and the strain-optic tensor of the optical fiber material; and $\vec{l}$ is the position in the fiber. The total phase induced is the result of the integration of refractive index perturbations along the optical fiber.

$$\Delta\phi(t) = k \int \Delta n(l, t)\, \mathrm{d}l \tag{3}$$

The phase shift can be increased using a longer fiber segment exposed to the acoustic wave. However, the use of large fiber arrangements at frequencies of

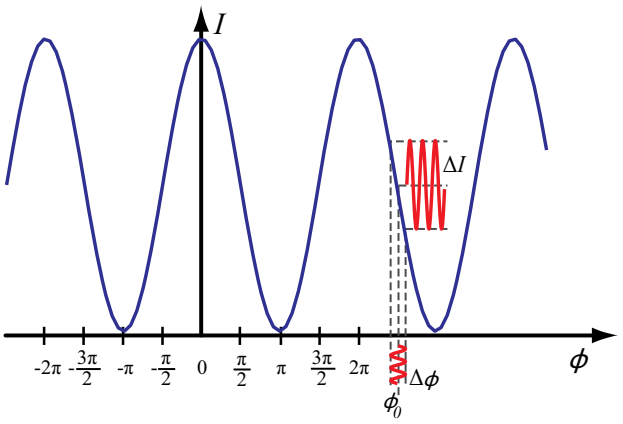


**Figure 1** Mach-Zenhder interferometric transfer function and response of the interferometer to a perturbation around the quadrature point.

1 MHz cause a temporal average of the ultrasonic signal, this is because the acoustic wavelength is close to 1.5 mm. Thus, regarding the sensitivity at ultrasonic frequencies there is a trade-off between fiber length and temporal average.

The relation between the intensity of the light at the output of the Mach-Zehnder interferometer and the phase difference between both arms, which is represented in Figure 1, is given by

$$I = I_r + I_m + 2\sqrt{I_r I_m}\cos\Delta\phi \tag{4}$$

where $I_r$ and $I_m$ are the intensities of the reference and measurement arms respectively. It has been assumed that the coherence length is much longer than the path difference between both arms and that the light at their output has the same polarization state. To use the interferometer arrangement as a sensor it is necessary to establish an operating point to obtain constant sensitivity and linearity. This can be achieved by using a phase stabilization device [15] that fixes the operating point to the region of the maximum slope in the transfer function (i.e. quadrature point). In this position of quadrature, if the acoustically induced phase shift is small, $\Delta\phi \ll 1$, the interferometric sensitivity is

$$\left|\frac{\Delta I}{\Delta\phi}\right| = 2\sqrt{I_r I_m}$$

In the case of $I_r = I_m$, the interferometric sensitivity is simplified to $|\Delta I/\Delta\phi| = 2I_m$.

## 3. Optical fiber sensor design

### *3.1 Sensitivity characterization of the fiber optic sensor*

The sensitivity per unit length is a key parameter for designing the optical fiber arrangement. To evaluate it we measured the phase shift induced in the optical fiber using ultrasonic waves generated from a calibrated piezoceramic (PZT) emitter. The characterization setup is presented in Figure 2a. A Mach-Zehnder interferometer was used to obtain the phase induced on a segment of the optical fiber under test. Water was used to ensure consistent and repeatability acoustic coupling between the emitter and the optical fiber segment. In the reference arm a phase modulator, formed from a fiber coil wrapped around a cylindrical PZT, has been employed to obtain the interferometric visibility at the time of measurement. The output of the interferometer is measured using an avalanche photodiode module

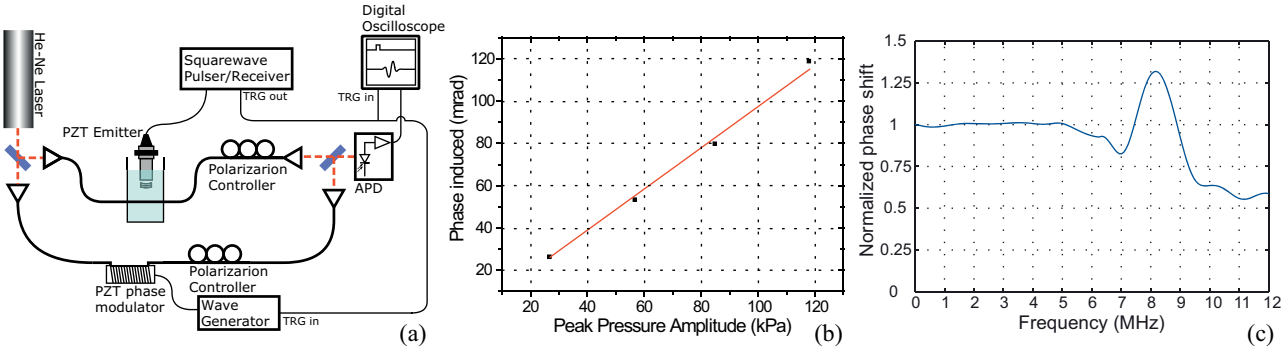


**Figure 2** (**a**) Experimental setup for sensitivity characterization of the optical fiber sensor. The light from a He-Ne laser (632.8 nm) is introduced in the fiber optic Mach-Zehnder interferometer. The polarization controllers are used to guarantee equal state of polarization at the output of both arms maximizing the visibility of the interference. The calibrated PZT emitter and the optical fiber are inside a tank filled with water to ensure a consistent acoustic coupling. The PZT phase modulator is used to register the visibility of the interference at the same time of the ultrasonic signal measurement in order to precisely recover the optical phase induced. (**b**) Relation between 1 MHz pulse amplitude pressure and phase shift induced in the single mode SOF. (**c**) Normalized frequency response of fiber optic sensor to normally incident ultrasonic wave.

(Hamamatsu C5331) and monitored using a digital oscilloscope. The bandwidth of this optical detector is 100 MHz, with a lower cut off frequency of 4 kHz. The signal captured from the oscilloscope is sent to a computer for post processing to obtain the phase. Immersion transducers from Panametrics with central resonant frequencies of 1 MHz and 10 MHz were used as ultrasonic emitters. These transducers were excited using a square pulse generator (Panametrics 5077PR). The amplitude of the square pulse was varied between 100 V and 400 V in steps of 100 V. The oscilloscope and the wave generator which feed the phase modulator were synchronized with the square pulse generator.

In our experiments we have used a single-mode silica optical fiber (SOF) (SCSM-633-HP, Stocker-Yale Inc., Salem, NH, USA). We have measured ultrasonic signals which have been produced by the PZT emitters using a single-mode SOF. Figure 2b represents the phase induced in the single-mode SOF from the 1 MHz ultrasonic PZT emitter for voltages ranging from 100 V to 400 V. These phase signals have been obtained by demodulation of the interferometric signals and have been digitally filtered using a high pass filter with a cutoff frequency of 0.3 MHz to remove the reference arm signal. The measured frequency response of the fiber sensor to a perpendicularly incident ultrasound is shown in Figure 2c, having a bandwidth that exceeds 10 MHz. It has been deconvolved from the response of the system to the ultrasonic waves generated using the 10 MHz transducer. This transducer was previously calibrated with a 100 MHz wideband ultrasonic calibrated sensor (WAT-13, Fairway Medical Technologies, Houston, TX, USA).

At the working frequency of 1 MHz the acoustic sensitivity of the SOF is measured to be $0.95 \pm 0.03$ mrad/kPa and at 10 MHz is $0.87 \pm 0.11$ mrad/kPa. The acoustic beam diameter was close to 3.4 mm at the measurement distance, which is shorter than the length of the segment under test, thus the sensitivity at 1 MHz per unit length is 0.28 mrad/kPa/mm. The sensor with an active fiber length of 100 mm and an interferometric system with a resolution of 5 mrad has a noise equivalent pressure (NEP) of 0.18 kPa at 1 MHz.

### 3.2 *Detection of optoacoustic generated signals*

The ultrasonic transducer designed for optoacoustic generation signals is composed of a single layer coil with 20 loops of single mode optical fiber at 633 nm. The sensor is placed on the surface of the medium being imaged with a small acoustic contact area. The active sensor length is 100 mm and only corresponds to the contact area between the phantom and the coil, given that ultrasonic waves cannot reach the rest of the fiber.

We have compared the optoacoustic signal detection using the the optical fiber sensor to those from a wideband ultrasonic PVDF transducer. The optoacoustic signal was produced irradiating a large cylindrical phantom [16] (dia. = 14.5 cm, h. = 8.5 cm) made of poly(vinyl-chloride) plastisol (PVCP) with optical pulses generated from a Nd-YAG laser (Quantel ULTRA). The phantom mimics optical and acoustic properties of biological soft tissues has an optical absorption coefficient $\mu_a = 0.12\ \mathrm{cm}^{-1}$, an effective scattering coefficient of $\mu_s' = 5.4\ \mathrm{cm}^{-1}$ and an anisotropy factor of $g = 0.8$ at 1064 nm. Embedded at approximately 20 mm below the surface of the phantom is a bar shaped optically absorbing object of dimensions $220.7\ \mathrm{cm}^3$ with $\mu_a = 0.58\ \mathrm{cm}^{-1}$. The Nd-YAG laser emits pulses at the wavelength of 1064 nm with 75 mJ of energy, temporal duration of 6 ns and a repetition rate of 10 Hz.

Figure 3a shows the fiber optic Mach-Zehnder interferometer sensor experimental setup. The light from a He-Ne laser, which is linearly polarized and emits at a wavelength of 632.8 nm, is divided using a 50/50 optical beam splitter and coupled into two silica optical fibers (i.e. the reference and measurement arm of the fiber optic interferometer). The optical fiber sensor is in the measurement arm of the interferometer. This sensor is placed on the surface of the phantom and has a contact area of $0.5\ \mathrm{cm}^2 \times 0.5\ \mathrm{cm}^2$. In the reference arm the phase modulator uses a feedback loop to stabilize the interferometer at the quadrature point thus compensating temperature drifts and low frequency vibrations. The interference visibility is optimized by matching the polarization at the output of each fiber arm using polarization controllers. The interferential optical signal is measured using the same APD module and digital oscilloscope as before.

The phantom lies over an array of 64 PVDF wideband detectors arranged in a concave arc (Figure 3b and c, this forms part of an optoacoustic probe supplied as a component of the Laser Optoacoustic Imaging System (LOIS, Fairway Medical Technologies, Houston, TX, USA) [14]. Each sensor of the array system has a sensitivity of 1.66 mV/Pa at a frequency of 1.5 MHz after two stages of 20 dB amplification. The fiber optic sensor is placed directly opposite the PVDF transducer which is located in the center of the arc shaped array. The absorber inside the phantom is located approximately equidistant between both electronic and optical sensors.

Figure 4a depicts a typical optoacoustic signal detected from an absorbing object with a rectangular bar shape and positioned at an angle to a sensor channel of the PVDF array. The voltage signal ob-

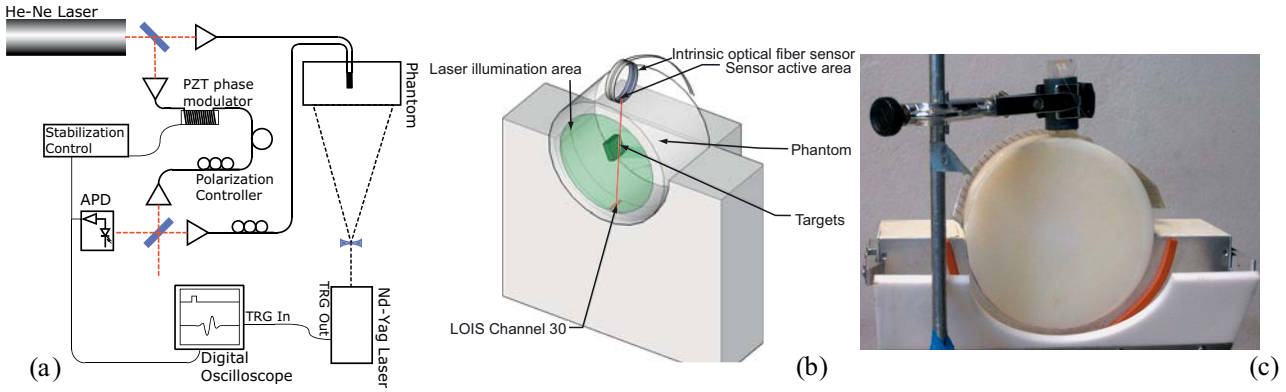


**Figure 3** (**a**) Optoacoustic experimental setup for comparison of fiber opic and piezoelectric transducers. (**b**) Schematic diagram showing cylindrical phantom placed in a hemi-cylindrical cup of an arcshaped array of PVDF transducers and a fiber optic sensor located on the top. (**c**) Photograph of a cylindrical PVCP phantom placed at the top of the cylindrical phantom with a fiber optic sensor attached at the top. The fiber optic sensor has a contact area of $5 \times 5$ mm. The piezoelectric elements of the PVDF array have dimensions of $0.1 \times 2 \times 20$ mm.

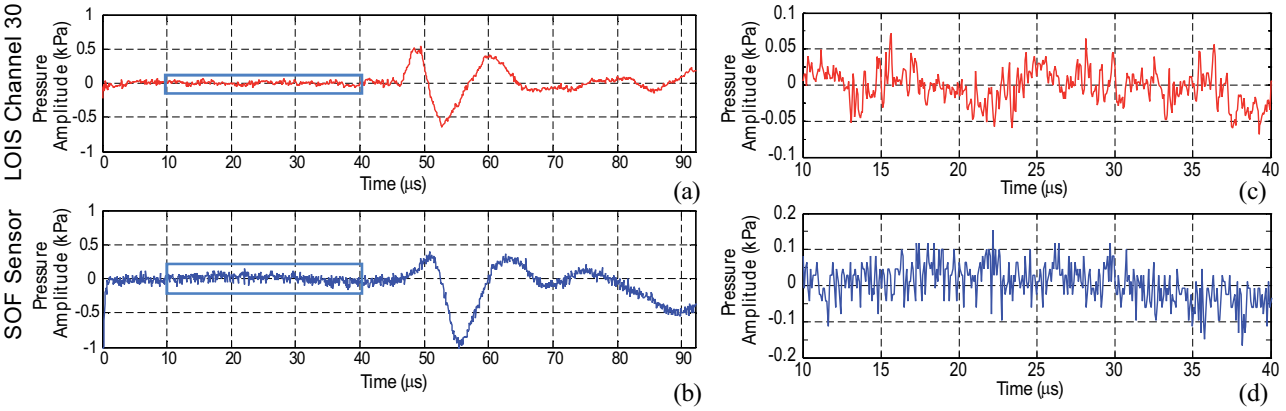


**Figure 4** (**a**) Optoacoustic signal received by channel 30 of PZT array expressed in pressure units. (**b**) Signal detected by an extrinsic fiber optic sensor at the same time but on the opposite side of the phantom. (**c**) and (**d**) magnification of the noise that correspond to the marked areas in the Figures (a) and (b) respectively.

tained was deconvolved to pressure using the known impulse response of the PVDF detector [14]. Figure 4b shows the interferometric signal of the intrinsic fiber optic sensor. Comparing Figures (a) and (b), a similar pulse shape and time of flight as detected with two different sensors can be observed. Note that the absorbing object is close to the center of the phantom, but its position is not necessarily symmetric with respect to the two ultrasonic sensors. The temporal width of the pulse is related to the spatial dimension of the absorber in the direction perpendicular to the sensor surface. A sharp negative pulse at the origin in the fiber optic sensor signal was due to the scattered light from the Nd : YAG laser pulses incident on the APD photodetector. This pulse can be used as a trigger to accurately synchronize an array of optoacoustic sensors. Figure 4c and d show the noise characteristic that the sensors present during the optoacoustic acquisition. The noise levels for the PVDF transducer is about 50 Pa and in the case of the optical fiber sensor is about 100 Pa. In the former case the electronic bandwidth is limited to 2.5 MHz, however in the last case it is limited by the digital oscilloscope low pass filter to 20 MHz.

## 4. Optoacoustic image reconstruction algorithm

### *4.1 Optoacoustic tomography (OAT)*

In optoacoustic excitation, if the laser pulse is short enough so that the the heat conduction is negligible during the laser pulse (thermal confinement) and the stress waves are longer than the duration of the

 

pulse travelling through the characteristic dimension of the heated region (stress confinement), then the initial pressure distribution is proportional to the optical absorption coefficient and the optical fluence. The initial pressure distribution excited by a laser pulse $L(t)$ in a random and heterogeneous optically absorbing and scattering tissue equals $p_o(\vec{r}')$. Assuming a delta-pulse excitation (i.e., $L(t) = \delta(t)$), the optoacoustic pressure $p_\delta(\vec{r}, t)$ at position $\vec{r}$ and time $t$ initiated by source $p_o(\vec{r}')$ can be computed using the following equation [17]:

$$p_\delta(\vec{r}, t) = \frac{1}{4\pi v_s^2} \frac{\partial}{\partial t} \left[ \frac{1}{v_s t} \iiint p_o(\vec{r}')\, \delta\left( t - \frac{|\vec{r}' - \vec{r}|}{v_s} \right) \mathrm{d}\vec{r}' \right] \tag{5}$$

where $v_s$ (in mm/us) is the speed of sound in tissue. The Eq. (5) essentially computes the acoustic pressure at position $\vec{r}_o$ and time $t = |\vec{r}' - \vec{r}|/v_s$ integrating the initial pressure distribution $p_o(\vec{r}')$ over the surface of a sphere of radius $|\vec{r}' - \vec{r}|$ (see Figure 5). For a finite pulse duration, $p(\vec{r}, t)$ is defined by the following convolution [17]:

$$p(\vec{r}, t) = \int_{-\infty}^{+\infty} L(t - \tau)\, p_\delta(\vec{r}, \tau)\, \mathrm{d}\tau \tag{6}$$

where $p_\delta(\vec{r}, t)$ is the impulse-heated optoacoustic pressure and $L(t)$ is the temporal profile of the laser pulse.

The acoustic pressure at position $r$ at time $t$ can be calculated integrating the initial pressure distribution $p_o(\vec{r}')$ on a spherical surface with radius $|\vec{r}' - \vec{r}| = v_s t$.

Therefore, the goal of OAT is to invert Eq. (5) to recover the initial pressure distribution $p_o(\vec{r}')$ that requires computer-based reconstruction algorithms.

## 4.2 Exact time-domain back-projection algorithm

Xu and Wang have derived an exact time-domain back-projection reconstruction formula based on measured pressure transients for the three types of imaging geometries: planar, cylindrical and spherical [18]. Nevertheless, in practical applications, the measurement surfaces are finite and partially enclose the region under test, thus the OA signals cannot be collected from all directions. As a consequence of facing an incomplete data problem, the resulting OA image is not exact.

The exact back-projection algorithm can be written in a discrete form as:

$$p_o(\vec{r}') = \sum_{i=1}^{N} \Delta\Omega_i b\left( \vec{r}_i, t = \frac{|\vec{r}' - \vec{r}_i|}{v_s} \right) \Big/ \sum_{i=1}^{N} \Delta\Omega_i \tag{7}$$

where $p_o(\vec{r}')$ is the initial pressure distribution to be reconstructed, $N$ is the total number of detection positions, $b(\vec{r}_i, t)$ is the back-projection term related to the signal $p(\vec{r}_i, t)$ and the ratio $\Delta\Omega_i / \sum(\Delta\Omega_i)$ is the solid angle weighting factor, which compensates the reconstruction distortion resulting from the limited view.

The back-projection term, $b(\vec{r}_i, t)$, can be calculated as follows:

$$b(\vec{r}_i, t) = 2p(\vec{r}_i, t) - 2t \frac{\partial p(\vec{r}_i, t)}{\partial t} \tag{8}$$

The solid-angle element related to the measurement at position $\vec{r}_i$ depends on the detection geometry and obeys:

$$\Delta\Omega_i = \frac{\Delta S_i}{|\vec{r}' - \vec{r}_i|^2} \left( \vec{n}_i^s \frac{\vec{r}' - \vec{r}_i}{|\vec{r}' - \vec{r}_i|} \right) \tag{9}$$

where $\vec{n}_i^s$ is a unitary vector normal to the measurement surface pointing to the source.

The exact BP formula can be computed using the following steps: (1) calculate the back-projection term $b(\vec{r}_i, t)$ for each OA signal $p(\vec{r}_i, t)$, (2) back-project it over spherical shells (radial BP), (3) sum over all the projections, and (4) normalize each pixel of the reconstructed volume with the summation of $\Delta\Omega_i$ of each back-projection step.

The exact BP formula in practical applications produces images with excellent resolution (sharp boundaries) but poor contrast. As a solution to this problem, some approximate time-domain filtered back-projection reconstruction algorithms have also been reported [14].

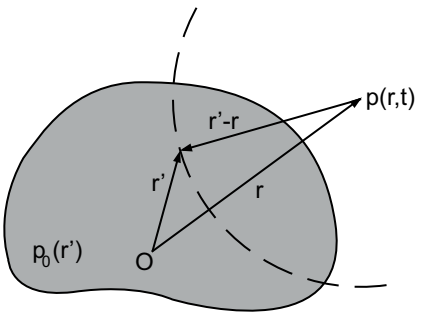


**Figure 5** Schematic diagram of the optoacoustic signal generation.

## 4.3 Wavelet-filtered time-domain back-projection algorithm

In order to sharpen object boundaries while simultaneously preserving high contrast of the reconstructed objects, a wavelet transform implementation using a wavelet family resembling the theoretical $N$-shaped OA signal has been used [14]. The wavelet transform

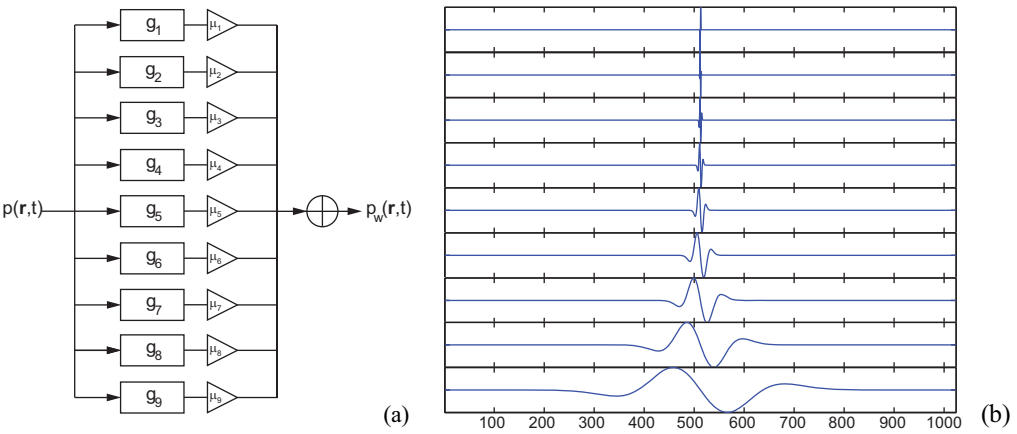


**Figure 6** (**a**) Schematic diagram of the wavelet-based bank of filters; (**b**) nine scales of the 3-rd derivative of the Gaussian wavelet covering a range of frequencies from $k = 4$ to 1024 digital samples: $g_1(t)$, $g_2(t)$, …, $g_9(t)$.

has been established in signal processing as an exceptional tool for localization of the specified signal profiles [19]. Images are obtained first using multiresolution wavelet-based signal processing on the OA signals and subsequently using a radial BP algorithm.

Nine scales of the same wavelet covering a wide range of frequencies from $k = 4$ to 1024 digital samples are generated: $g_1(t)$, $g_2(t)$, …, $g_9(t)$ (Figure 6). Oraevsky et al. used the 3-rd derivative of the Gaussian wavelet family as the wavelet is similar to the theoretical *N*-shaped OA signal to be enhanced after signal processing.

The filtered OA signal $p_w(\vec{r}, t)$ can be written as:

$$p_w(\vec{r}, t) = \sum_{i=1}^{9} \mu_i^{\mathrm{HF}} g_i(t) * p(\vec{r}, t) \qquad (10)$$

where $g_i(t)$ is one of the nine wavelet scales and $\mu^{\mathrm{HF}}$ is a weighting factor designed to enhance high frequencies components of the signal. Here, we use:

$$\mu^{\mathrm{HF}} = (1024, 512, 256, 128, 64, 32, 16, 8, 4) \qquad (11)$$

Thus, the filtered back-projection formula consists of three steps: (1) compute $p_w(\vec{r}, t)$ for each OA signal $p(\vec{r}, t)$, (2) perform a radial back-projection of each filtered signal, and (3) sum over all the projections.

## 5. Optoacoustic image reconstruction

We have reconstructed optoacoustic images from the pressure signals measured by the optical fiber sensor and PVDF transducers from the LOIS array. In order to reconstruct a two-dimensional image, the fiber optic sensor was placed in contact with the upper part of the PVCP phantom, which was rotated to 58 different positions, forming a total scanned array aperture of 178°. The phantom was illuminated using an OPO laser (Vibrant 355, OPOTEK Inc., Carlsbad, CA, USA) tuned to 480 nm which delivers, at a distance of 125 cm, an elliptical laser spot with a major axis of 2.4 cm and minor axis of 0.8 cm and a fluence of 20 mJ/cm$^2$. The second optoacoustic image was reconstructed using signals acquired from the LOIS system detected using 64 piezoelectric PVDF transducers which occupy the total angular aperture of 174°. In this case, the phantom was illuminated using a Q-switched Nd : YAG. In both cases we have used the radial back-projection algorithm for the reconstruction of the optoacoustic images [20], reviewed in the previous section. Digitized optoacoustic signals detected by our optical fiber sensor were filtered using a band-pass filter which has a cut off frequency of 30 kHz and 2 MHz. These signals were registered without any temporal averaging. The optoacoustic signals, detected using the LOIS, were filtered using a 9 scale wavelet filter that simultaneously converts the bipolar pressure signals to monopolar signals of absorbed energy [14]. Figure 7 shows the position of the absorbing object in the phantom (Figure 7a) and the reconstructed images using both systems, Figure 7b depicts a LOIS image

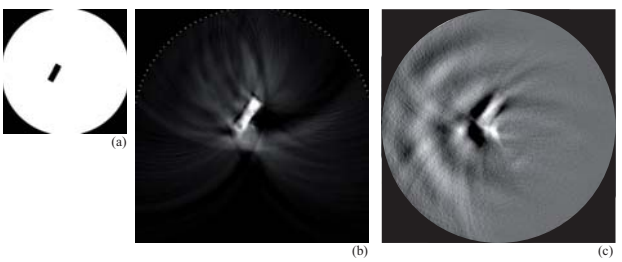


**Figure 7** (**a**) Diagram showing location of the embedded object in the PVCP phantom. (**b**) Optoacoustic image obtained from LOIS utilizing an array of 64 PVDF transducers. (**c**) Optoacoustic image reconstructed from fiber optic sensor signals.

**Table 1** Acoustic sensitivity for 1 and 10 MHz emitters of single mode SOF, single mode POF and GIPOF-50.

| Frequency (MHz) | SM-SOF (mrad/kPa) | SM-POF (mrad/kPa) | GIPOF50 (mrad/kPa) |
|---|---|---|---|
| 1 | $0.95 \pm 0.03$ | $13.07 \pm 0.28$ | $13.81 \pm 0.18$ |
| 10 | $0.87 \pm 0.11$ | $4.07 \pm 0.16$ | $3.98 \pm 0.13$ |

and Figure 7c depicts an image reconstructed using the signals obtained from the fiber optic sensor. The optoacoustic images generated by both systems are in good agreement when considering the dimensions, shape and location of the embedded object. Also, based on the shape of resolved corners, both systems possess similar spatial resolution.

## 6. Conclusion

An ultrasonic sensor based on an optical fiber interferometer has been designed, developed and calibrated. The system is capable of detecting wideband ultrasound signals over the frequency range from 0.1 to 10 MHz and has a noise equivalent pressure of ~100 Pa. The optoacoustic sensitivity can be further improved by selecting a more sensitive fiber optic material [21]. By employing a polymer optical fiber (POF) in place of the silica optical fiber as the sensing element, we have measured an increase in ultrasonic sensitivity by more than 5 times over all the sensor bandwidth (Table 1). Based on these new results, we expect to improve the constrast and detection capability of the optoacoustic imaging system by using these polymer optical fibers.

We have reconstructed a cross sectional image of an absorbing object within a high scattering media using our optical fiber sensor in a semi-circular scanning configuration. Results are comparable to those obtained with a system based on broadband piezoelectric transducers. The experiments in the breast tissue mimicking phantom attempt to demonstrate the feasibility of the interferometric fiber optic sensors developed for biomedical applications, particularly in optoacoustics imaging. Further work will be dedicated to improve the sensitivity of the fiber optic sensors by using polymer optical fiber and by increasing the density of the sensor active area, and implement wavelet filtering for the optoacoustic signal processing. This will result in an improved signal-to-noise ratio and, in turn, contrast of optoacoustic images. Finally, it is essential to improve the scanning system, this will reduce data collection time. Also, it is projected that future experimental trials will be performed using a parallel multi-channel interferometric sensor system.

**Horacio Lamela** received the Industrial Engineering degree from the Universidad Politécnica de Madrid (UPM) in 1980, the "Diplome d'Etudes Approfondies" (DEA) from the University of Paris XI in 1981, and the "Docteur-Ingenieur" degree in optical interferometry from the Conservatoire d'Arts et Metiers of Paris, 1985, France. From 1985 to 1987, he was with the Massachusetts Institute of Technology, Cambridge, as a Postdoctoral Fellow with the Electrical Engineering and Computer Sciences Department and Visiting Scholar at the Research Laboratory of Electronics. He is presently a full Professor with the Departamento de Tecnologia Electronica and leader of the Optoelectronics and Laser Technology Group (GOTL) at Universidad Carlos III de Madrid, Spain. His research interests are high-speed semiconductor lasers dynamics and picosecond gain-switching diode lasers, dual mode diode lasers for mmW and THz generation, laser optoacoustics with gold nanoparticles for spectroscopy and biomedical applications and interferometric fiber optic sensor for optoacoustic biomedical imaging.

**Daniel Gallego** received the B.Sc. degree in physics and the M.Sc. degree in optoelectronics from the Universidad de Santiago de Compostela (USC), Spain in 2000 and 2002 respectively. In 2004 he joined to the GOTL group from Universidad Carlos III de Madrid to study the Bragg gratings as ultrafast mode-locking diode laser pulse compressor devices in the framework of the European project IST-MONOPLA. There he obtained the DEA in electronic, electric and automatic engineering. He is currently working toward the Ph. D. degree in the same group. His research interest includes optical sensors for detecting ultrasound, fiber optic interferometry, optoacoustic signal generation, optoacoustic imaging reconstruction algorithms and biomedical imaging.

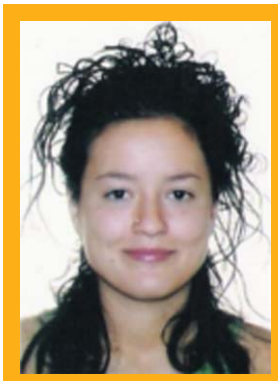

**Rebeca Gutiérrez** received the Telecommunication Engineering degree from the Universidad Carlos III de Madrid, Spain, in 2008. In 2007 she joined the GOTL as a trainee researcher, where she did her master's thesis project in image reconstruction algorithms for optoacoustic medical imaging. She joined Argongra in 2009 and is currently working in the R&D Department as a research engineer in projects related with satellite image processing and design, development and integration of geographical information systems. Since 2010, she is also working toward the M.Sc. and Ph.D. degree at the Universidad Politécnica de Madrid (UPM). Her research interests include remote sensing systems, image processing, computer vision and data mining.

**Alexander A. Oraevsky** received his initial training in physics and mathematics from the Moscow Physical and Engineering Institute in Moscow, Russia and obtained a doctorate in laser spectroscopy and laser biophysics from the USSR Academy of Sciences. He began his pioneering research in the field of optoacoustic imaging, sensing and monitoring in 1988. In 1992, as Whitaker Fellow, he joined the faculty at Rice University. Prior to joining Fairway Medical Technologies as Vice-President of Research and Development, he was the Director of the Optoacoustic Imaging and Spectroscopy Laboratory at the University of Texas Medical Branch in Galveston, TX and an Assistant Professor at the Department of Ophthalmology and Visual Sciences. Presently he holds an adjunct Professor position at the Biomedical Engineering Department of the University of Houston.

## References

[1] A. A. Oraevsky, S. L. Jacques, and F. K. Tittel, Proc. SPIE **1882**, 86–101 (1993).
[2] L. H. V. Wang, Photoacoustic Imaging and Spectroscopy (CRC Press, 2009).
[3] J. Laufer, D. Delpy, C. Elwell, and P. Beard, Phys. Med. Biol. **52**, 141–168 (2007).
[4] A. A. Oraevsky, E. V. Savateeva, S. V. Solomatin, A. A. Karabutov, V. G. Andreev, Z. Gatalica, T. Khamapirad, and P. M. Henrichs, Proc. SPIE **4618**, 81–94 (2002).
[5] S. Manohar, A. Kharine, J. C. G. Van Hespen, W. Steenbergen, and T. G. Van Leeuwen, Phys. Med. Biol. **50**, 2543–2557 (2005).
[6] S. Manohar, S. E. Vaartjes, J. C. G. Van Hespen, J. M. Klaase, F. M. Van Den Engh, W. Steenbergen, and T. G. Van Leeuwen, Opt. Express **15**, 12277–12285 (2007).
[7] X. D. Wang, Y. J. Pang, G. Ku, X. Y. Xie, G. Stoica, and L. H. V. Wang, Nat. Biotechnol. **21**, 803–806 (2003).
[8] H. F. Zhang, K. Maslov, M. Sivaramakrishnan, G. Stoica, and L. H. V. Wang, Appl. Phys. Lett. **90**, 053901 (2007).
[9] E. Zhang, J. Laufer, and P. Beard, Appl. Optics **47**, 561–577 (2008).
[10] P. Fomitchov and S. Krishnaswamy, Opt. Eng. **42**, 956–963 (2003).
[11] V. Wilkens and C. Koch, Opt. Lett. **24**, 1026–1028 (1999).
[12] R. De Paula, J. H. Cole, and J. A. Bucaro, J. Lightwave Technol. **1**, 390–393 (1983).
[13] H. Wen, D. G. Wiesler, A. Tveten, B. Danver, and A. Dandridge, Ultrason. Imaging **20**, 103–112 (1998).
[14] S. A. Ermilov, T. Khamapirad, A. Conjusteau, M. H. Leonard, R. Lacewell, K. Mehta, T. Miller, and A. A. Oraevsky, J. Biomed. Opt. **14**, 024007-1–14 (2009).
[15] D. A. Jackson, R. Priest, A. Dandridge, and A. B. Tveten, Appl. Optics **19**, 2926–2929 (1980).
[16] G. M. Spirou, A. A. Oraevsky, I. A. Vitkin, and W. M. Whelan, Phys. Med. Biol. **50**, N141–N153 (2005).
[17] L. V. Wang, IEEE J. Sel. Top. Quantum Electron. **14**(1), 171–179 (2008).
[18] M. Xu and L. V. Wang, Phys. Rev. E Stat Phys Plasmas Fluids Relat. Interdiscip. Topics **71**, 016706 (2005).
[19] G. Strang and T. Nguyen, Wavelets and filter banks, (Wellesley-Cambridge Press, USA, 1996).
[20] R. A. Kruger, D. R. Reinecke, and G. A. Kruger, Med. Phys. **26**, 1832–1837 (1999).
[21] D. C. Gallego and H. Lamela, Opt. Lett. **34**, 1807–1809 (2009).

 